Numerical Methods to Solve Elasticity Problems with Point Sources

Peng, Qiyao; Vermolen, F.J.

Publication date
2019

Document Version
Final published version

Citation (APA)
Peng, Q., & Vermolen, F. J. (2019). *Numerical Methods to Solve Elasticity Problems with Point Sources*. (Reports of the Delft Institute of Applied Mathematics; Vol. 19-02). Delft University of Technology.

DELFT UNIVERSITY OF TECHNOLOGY

REPORT 19-02

Numerical Methods to Solve Elasticity Problems with Point Sources

Q. Peng, F.J. Vermolen

ISSN 1389-6520

Reports of the Delft Institute of Applied Mathematics

Delft 2019

Numerical Methods to Solve Elasticity Problems with Point Sources

Q. Peng, F.J. Vermolen

May 24, 2019

Abstract

During the wound healing processes of severe injuries, contractions are likely to deteriorate into contractures, which concur with disabilities of the patients. Elasticity equation, with point sources described by Dirac Delta distributions, is used to depict the mechanics taking place in the skin after the trauma. However, the existence of a Dirac Delta distribution results into a singularity of the solution. In other words, the solution does not lie in Hilbert Space. Hence, in this report, we use various approaches regarding the finite element methods in two and three dimensions by the motivation of improving the accuracy. As for the application, besides the alternatives aforementioned, there are multiple possibilities focusing on how to address point forces, that is, whether to treat the region covered by cell as part of the computational region. The idea develops into the immersed boundary approach and the hole approach, and the numerical results of these two approaches verify the consistency.

The growth of the number of cells in the computational domains requires both accuracy and efficient computation time. Hence, polygonal approximation of the cell is applied and various types of polygons are compared, and it is indicated that square is the most appropriate choice.

1 Introduction

For severe burn injuries, since they will cause extensive loss of soft tissue, secondary healing will occur[3]. In some cases, the large severe wound will reduce to 5-10% of its original area[3] due to the occurrence of contraction. Contractions arise in the third phase of wound healing processes (namely hemostasis, inflammation, proliferation and maturation/remodeling)[3].

Proliferation phase starts from day three and will continue for 2-4 weeks after wounding[3]. It includes epithelialization, fibroplasia, angiogenesis and the development of granulation tissue. Redifferentiation of the keratinocytes in the neo-epidermis is activated before completing wound closure and leads to efficient reconstitution of the epidermal barrier[4]. After epithelialization, injured dermis starts being repaired. Within four days, the clot will be broken by proteins like plasmins, of which the production is affected by the presence of tissue plasminogen activator (tPA). Then the clot is replaced by granulation tissue, which is the combination of cells and connective tissues[2]. Fibroblasts have been attracted to the wound area from the wound edge or the circulation by a number of factors like platelet-derived growth factor (PDGF) and transforming growth factor-β(TGF-β)[3]. When they enter the wound region, fibroblasts are mostly dividing into myofibroblats, which pull the extracellular matrix and thereby cause wound deformation[4]. In other words, wound contractions occur mainly due to myofibroblasts interacting with the surrounding extracellular matrix. The amount of the contraction is related to the size, shape, depth and anatomical location of the wound. For instance, tissues with

stronger laxity contract more comparing to loose tissues, and square-shaped wounds contract more than circular ones[5]. Due the occurrence of contraction, the exposed surface area of the wound is decreasing without production of new wound-covering tissues. Notably, contraction must be distinguished from contracture which is a pathological process of excess contraction and caused by the application of excessive stress to the wound. In other words, contractures usually occur with the disabilities of the patients in the meanwhile, which severely affect patients' life.

In the elasticity equation, a point source force, which is expressed by a Dirac Delta distribution, causes a singularity and thereby for dimensionality exceeding one the solution is not in the same Hilbert space as the basis functions for many naive finite-element strategies. In order to deal with matter, we study two approaches: a homogenization approach and a mixed approach. In the first approach, we mainly use Green's functions as an intermediary, while in the second one we reduce the order by rewriting the second-order PDE into a system of first-order PDEs.

The quest of several alternative methods is motivated by finding ways to improve accuracy, and by the need of efficiency to simulate the mechanical processes occurring in the skin after a serious (burn) trauma.

Apart from applications of various approaches regarding finite-element methods, there are various possibilities focusing on how to address point forces. To rephrase it, there are different approaches that treat point forces on the boundary of a cell. One may include the region covered by the cell as part of computational domain. This idea develops into the immersed boundary approach. Contrary, the hole approach, is based on excluding the cell from the computational domain and treat the cell forces as a boundary condition.

In this paper, all the aforementioned approaches are analysed. We will delve into the improvement of numerical performance, such as accuracy and convergence. Aside from that, computational efficiency will be taken into account, when determining which approach is elected under different circumstances and for various practical purposes.

The paper is structured as follows. In Section 2, we present the homogenization approach and mixed approach in both two and three dimensions. We investigate the 'hole approach' as well as the immersed boundary method. Section 3 displays numerical results with respect to the approaches stated in the aforementioned section to see if there is any improvement of the other two approaches compared to the direct approach. In Section 4, we compare immersed boundary approach to the hole approach. Furthermore, the conclusions and some directions for future research are presented in Section 5.

2 Mathematical Models

2.1 The Immersed boundary method in $\mathbb{R}^2$

The (myo)fibroblasts exert pulling forces on their immediate surroundings in the extracellular matrix. These forces are directed towards the cell centre and they cause local displacements and deformation of the extracellular matrix. The combination of all these forces cause a net contraction of the tissue around the region where the fibroblasts are actively exerting forces. Typically the fibroblasts, which are responsible for the regeneration of collagen, enter the wound area after serious trauma. Their migration towards the wound is triggered by a chain of chemical signals. Since after restoration of the collagen, the fibroblasts die as a result of apoptosis (programmed cell death), the forces that they exert on their environment disappear. Since the deformations are relatively large, residual stresses remain and hence permanent displacements remain. Therefore we consider two types of forces: temporary forces ($\boldsymbol{f}_t$) and plastic forces ($\boldsymbol{f}_p$). The way we treat the forces is formalized by Vermolen and Gefen.

For the temporary force of cell i, the cell boundary Γ^i is divided into line segments in the two-dimensional case. We assume that an inward directed force is exerted at the midpoint

of every line segment in the normal direction to the line segment. The total force is a linear combination of every force at every segment. Hence, at time t, the total temporary force is expressed by

$$\boldsymbol{f}_t = \sum_{i=1}^{T_N(t)} \sum_{j=1}^{N_S^i} P(\boldsymbol{x}, t)\boldsymbol{n}(\boldsymbol{x})\delta(\boldsymbol{x} - \boldsymbol{x}_j^i(t))\Delta\Gamma_N^{i,j}, \tag{2.1}$$

where $T_N(t)$ is the number of cells at time t, N_S^i is the number of line segments of cell i, $P(\boldsymbol{x}, t)$ is the magnitude of the pulling force exerted at point $\boldsymbol{x}$ and time t per length, $\boldsymbol{n}(\boldsymbol{x})$ is the unit inward pointing normal vector (towards the cell centre) at position $\boldsymbol{x}$, $\boldsymbol{x}_j^i(t)$ is the midpoint on line segment j of cell i at time t and $\Delta\Gamma_N^{i,j}$ is the length of line segment j.

Theoretically, when $N_S^i \to \infty$, i.e. $\Delta\Gamma_N^{i,j} \to 0$, Eq (2.1) becomes

$$\boldsymbol{f}_t = \sum_{i=1}^{T_N(t)} \int_{\partial\Omega_N^i} P(\boldsymbol{x}, t)\boldsymbol{n}(\boldsymbol{x})\delta(\boldsymbol{x} - \boldsymbol{x}_s^i(t))d\Gamma_N^i. \tag{2.2}$$

Here, $\boldsymbol{x}_s^i(t)$ is a point on the cell boundary of cell i at time t.

To describe the mechanics occurring, the equation for conservation of momentum over the computational domain Ω is used here:

$$-\nabla \cdot \underline{\underline{\sigma}} = \boldsymbol{f}.$$

In the above equation inertia has been neglected. We treat the computational domain as a continuous linear isotropic elastic domain. Therefore, we use Hooke's Law:

$$\underline{\underline{\sigma}} = \frac{E}{1+\nu}\left\{\underline{\underline{\epsilon}} + tr(\underline{\underline{\epsilon}})\left[\frac{\nu}{1-2\nu}\right]\underline{\underline{I}}\right\}, \tag{2.3}$$

where E is the Young's modulus of the domain, ν is Poisson's ratio and $\underline{\underline{\epsilon}}$ is the infinitesimal strain tensor, that is,

$$\underline{\underline{\epsilon}} = \frac{1}{2}\left[\nabla\boldsymbol{u} + (\nabla\boldsymbol{u})^T\right]. \tag{2.4}$$

The above PDE provides a good approximation if the displacements are relatively small. Further, we define the inner product of two second-order $n \times n$ tensors (matrices) $\underline{\underline{A}} and \underline{\underline{B}}$ as follows:

$$\underline{\underline{A}} : \underline{\underline{B}} = \sum_{i,j=1}^{n} a_{ij}b_{ij},$$

where a_{ij} and b_{ij} are the entries of $\underline{\underline{A}}$ and $\underline{\underline{B}}$, respectively.

2.1.1 The Direct Approach

On the outer boundary $\partial\Omega$, we use the following Robin boundary condition

$$\underline{\underline{\sigma}} \cdot \boldsymbol{n} + \kappa\boldsymbol{u} = \boldsymbol{0},$$

where κ is a positive constant representing spring force of the domain of computation with its far away surroundings and $\boldsymbol{u}$ denotes the displacement vector. Note that if $\kappa \to \infty$, then $\boldsymbol{u} \to \boldsymbol{0}$, and $\kappa \to 0$ represents a free boundary in the sense that no external force is exerted on the boundary.

For the case of only one cell i in the computational domain, we need to solve the following boundary value problem:

$$\begin{cases} -\nabla \cdot \underline{\underline{\sigma}} = \sum_{j=1}^{N_S^i} P(\boldsymbol{x},t)\boldsymbol{n}(\boldsymbol{x})\delta(\boldsymbol{x}-\boldsymbol{x}_j^i(t))\Delta\Gamma^{i,j}, & \text{in } \Omega, \\ \underline{\underline{\sigma}} \cdot \boldsymbol{n} + \kappa \boldsymbol{u} = \boldsymbol{0}, & \text{on } \partial\Omega. \end{cases} \tag{2.5}$$

Let $V(\Omega)$ be a completion of the Hilbert space $H^1(\Omega)$ with smooth functions[9], then the corresponding weak form of Eq (2.5) on Ω is

$$(WF_{\mathrm{I}}) \begin{cases} \text{Find } \boldsymbol{u} \in V(\Omega), \text{ such that} \\ \int_{\partial\Omega} \kappa \boldsymbol{u}\boldsymbol{\phi} d\Gamma + \int_\Omega \underline{\underline{\sigma}} : \nabla\boldsymbol{\phi} d\Omega = \int_\Omega \sum_{j=1}^{N_S^i} P(\boldsymbol{x},t)\boldsymbol{n}(\boldsymbol{x})\delta(\boldsymbol{x}-\boldsymbol{x}_j^i(t))\Delta\Gamma^{i,j}\boldsymbol{\phi} d\Omega \\ = \int_\Omega \int_{\partial\Omega_N^i} P(\boldsymbol{x},t)\boldsymbol{n}(\boldsymbol{x})\delta(\boldsymbol{x}-\boldsymbol{x}_j^i(t))\boldsymbol{\phi} d\Gamma^i d\Omega, \quad \text{as } N_S^i \to \infty \\ \text{for all } \boldsymbol{\phi} \in V(\Omega). \end{cases}$$

2.1.2 The Mixed Finite Elements Approach

Subsequently, we apply the mixed approach in the two dimensional case to solve the linear elasticity problem with the convolution of point forces that were described earlier. In three dimensional cases, we use the same principles. We use Hooke's Law for the relation between the stress and strain-tensors:

$$\begin{bmatrix} \sigma_{11} \\ \sigma_{22} \\ \sigma_{12} \end{bmatrix} = \frac{E}{(1+\nu)(1-2\nu)} \begin{bmatrix} 1-\nu & \nu & 0 \\ \nu & 1-\nu & 0 \\ 0 & 0 & 1-2\nu \end{bmatrix} \begin{bmatrix} \epsilon_{11} \\ \epsilon_{22} \\ \epsilon_{12} \end{bmatrix}, \tag{2.6}$$

or

$$\boldsymbol{\sigma} = \mathcal{C}\boldsymbol{\epsilon}.$$

We rewrite the expression above in the form of

$$\boldsymbol{\epsilon} = \mathcal{C}^{-1}\boldsymbol{\sigma},$$

where

$$\mathcal{C}^{-1} = \frac{1+\nu}{E} \begin{bmatrix} 1-\nu & -\nu & 0 \\ -\nu & 1-\nu & 0 \\ 0 & 0 & 1 \end{bmatrix}. \tag{2.7}$$

Hence, the PDE we are going to solve is

$$\begin{cases} \nabla \cdot \boldsymbol{\sigma}(\boldsymbol{x}) = -\sum_{j=1}^{N_S^i} P(\boldsymbol{x},t)\boldsymbol{n}(\boldsymbol{x})\delta(\boldsymbol{x}-\boldsymbol{x}_j^i(t))\Delta\Gamma^{i,j}, & \text{in } \Omega, \\ \boldsymbol{\sigma} = \mathcal{C}\boldsymbol{\epsilon}, & \text{in } \Omega, \\ \boldsymbol{n} \cdot \boldsymbol{\sigma} + \kappa \boldsymbol{u} = \boldsymbol{0}, & \text{on } \partial\Omega. \end{cases} \tag{2.8}$$

Let $W(\Omega)$ be a completion of $L^2(\Omega)$ containing sufficiently smooth functions[9], then the weak form for the general equation is

Find $(\boldsymbol{\sigma}, \boldsymbol{u}) \in W(\Omega) \times V(\Omega)$, such that

$$\int_\Omega \mathcal{C}^{-1}\boldsymbol{\sigma}(\boldsymbol{u}) : \underline{\underline{\tau}} - \boldsymbol{\epsilon}(\boldsymbol{u}) : \underline{\underline{\tau}} d\Omega = 0,$$

$$\int_\Omega \boldsymbol{\sigma}(\boldsymbol{u}) : \nabla\boldsymbol{\phi} d\Omega + \int_{\partial\Omega} \kappa \boldsymbol{u} \cdot \boldsymbol{\phi} d\Gamma = \int_\Omega \sum_{j=1}^{N_S^i} P(\boldsymbol{x}, t)\boldsymbol{n}(\boldsymbol{x})\delta(\boldsymbol{x} - \boldsymbol{x}_j^i(t))\Delta\Gamma^{i,j}\boldsymbol{\phi} d\Omega,$$

$$\forall(\underline{\underline{\tau}}, \boldsymbol{\phi}) \in W(\Omega) \times V(\Omega).$$

This is the mixed method developed by Hellinger and Reisner and this approach solves $(\boldsymbol{\sigma}, \boldsymbol{u})$, which is due to the fact that $\underline{\underline{\epsilon}}$ can be written as $\nabla^{(s)}(\boldsymbol{u})$; see [1] for more details.

2.2 Mechanics with One Point Source in $\mathbb{R}^3$

2.2.1 Direct Approach

We consider an open and bounded computational domain Ω with boundary $\partial\Omega$. Then the following PDE is used to describe the balance of momentum with one point source:

$$-\nabla \cdot \underline{\underline{\sigma}} = \boldsymbol{F}\delta(\boldsymbol{x} - \boldsymbol{x_0}) \text{in } \Omega, \tag{2.9}$$

where $\underline{\underline{\sigma}}$ is the Cauchy stress tensor and the right-hand side represents the force $\boldsymbol{F}$ exerted at point $\boldsymbol{x_0}$.

Using a spring force between the boundary of the domain of computation and its far away environment, we arrive at the following boundary value problem:

$$\begin{cases} -\nabla \cdot \underline{\underline{\sigma}}(\boldsymbol{u}) = \boldsymbol{F}\delta(\boldsymbol{x} - \boldsymbol{x_0}), & \text{in } \Omega, \\ \underline{\underline{\sigma}}(\boldsymbol{u}) \cdot \boldsymbol{n} + \kappa\boldsymbol{u} = \boldsymbol{0}, & \text{on } \partial\Omega. \end{cases} \tag{2.10}$$

where κ is a positive constant representing spring force. The corresponding weak form of Eq (2.10) is

Find $\boldsymbol{u} \in V(\Omega)$, such that

$$\int_{\partial\Omega} \kappa\boldsymbol{u}\boldsymbol{\phi} d\Gamma + \int_\Omega \underline{\underline{\sigma}}(\boldsymbol{u})\nabla\boldsymbol{\phi} d\Omega = \boldsymbol{F}\boldsymbol{\phi}(\boldsymbol{x_0}), \forall\boldsymbol{\phi} \in V(\Omega).$$

2.2.2 Homogenization Approach

Considering the same elasticity equation in $\mathbb{R}^3$, i.e.

$$-\nabla \cdot \sigma(\boldsymbol{u}) = \boldsymbol{F}\delta(\boldsymbol{x} - \boldsymbol{x_0}), \tag{2.11}$$

we search the solutions on an unbounded domain that vanish 'far away'. These expressions are also known as Green's functions. According to Weinberger et al., in three-dimensions, the Green's function is

$$G_{ij}(\boldsymbol{x}) = \frac{1}{16\pi\mu(1-\nu)\|\boldsymbol{x} - \boldsymbol{x_0}\|}\left((3-4\nu)\delta_{ij} + \frac{(x_i - x_{0_i})(x_j - x_{0_j})}{\|\boldsymbol{x} - \boldsymbol{x_0}\|}\right),$$

where μ and ν is the second Lamé parameter and the Poisson ratio. The displacement vector can be expressed by

$$\hat{u}_i(\boldsymbol{x}) = \sum_{j=1}^{3} G_{ij}(\boldsymbol{x}-\boldsymbol{x_0})F_j = \sum_{j=1}^{3} \frac{F_j}{16\pi\mu(1-\nu)\|\boldsymbol{x}-\boldsymbol{x_0}+\gamma\|}\left((3-4\nu)\delta_{ij} + \frac{(x_i - x_{0_i})(x_j - x_{0_j})}{\|\boldsymbol{x}-\boldsymbol{x_0}+\gamma\|}\right) \tag{2.12}$$

where i, j represent different coordinate directions and $\boldsymbol{x_0}$ is the source point. Here, we add γ, a very small positive constant in the dominator to prevent divisions by zero. We rewrite the problem by setting $\boldsymbol{v} = \boldsymbol{u} - \hat{\boldsymbol{u}}$, where $\boldsymbol{u}$ is the solution, being the displacement vector from Eq (2.10) and $\hat{\boldsymbol{u}} = [\hat{u}_x\ \hat{u}_y\ \hat{u}_z]^T$ is determined by Eq (2.12). Subsequently, by subtracting Eq (2.11) from Eq 2.10, we obtain the new PDEs as

$$\begin{cases} -\nabla \cdot \underline{\underline{\sigma}}(\boldsymbol{v}) = \boldsymbol{0} & \text{in } \Omega \\ \underline{\underline{\sigma}}(\boldsymbol{v}+\hat{\boldsymbol{u}}) \cdot \boldsymbol{n} + \kappa(\boldsymbol{v}+\hat{\boldsymbol{u}}) = \boldsymbol{0} & \text{on } \partial\Omega \end{cases} \tag{2.13}$$

The corresponding weak form is

$$\text{Find } \boldsymbol{v} \in H^1(\Omega), \text{ such that}$$

$$\int_{\partial\Omega} \kappa \boldsymbol{v}\boldsymbol{\phi} d\Gamma + \int_{\Omega} \underline{\underline{\sigma}}(\boldsymbol{v}) : \nabla\boldsymbol{\phi} d\Omega = -\int_{\partial\Omega} \underline{\underline{\sigma}}(\hat{\boldsymbol{u}}) \cdot \boldsymbol{n}\boldsymbol{\phi} d\Gamma + \int_{\Omega} \kappa\hat{\boldsymbol{u}}\boldsymbol{\phi}, \quad \forall\boldsymbol{\phi} \in H^1(\Omega).$$

2.2.3 Mixed Approach

Before we introduce the method, we rewrite Eq (2.3) and Eq (2.4) into a component-wise form such that the vector representation of $\underline{\underline{\sigma}}$ can be expressed by a matrix multiplying the vector representation of $\underline{\underline{\epsilon}}$. Since both $\underline{\underline{\sigma}}(\boldsymbol{u})$ and $\underline{\underline{\epsilon}}(\boldsymbol{u})$ are symmetric, we have six different entries in the three dimensional case. Therefore, the equation can be written as

$$\begin{bmatrix} \sigma_{11} \\ \sigma_{22} \\ \sigma_{33} \\ \sigma_{12} \\ \sigma_{13} \\ \sigma_{23} \end{bmatrix} = \frac{E}{(1+\nu)(1-2\nu)} \begin{bmatrix} 1-\nu & \nu & \nu & & & \\ \nu & 1-\nu & \nu & & 0 & \\ \nu & \nu & 1-\nu & & & \\ & & & 1-2\nu & & \\ & 0 & & & 1-2\nu & \\ & & & & & 1-2\nu \end{bmatrix} \begin{bmatrix} \epsilon_{11} \\ \epsilon_{22} \\ \epsilon_{33} \\ \epsilon_{12} \\ \epsilon_{13} \\ \epsilon_{23} \end{bmatrix} \tag{2.14}$$

or

$$\boldsymbol{\sigma} = \mathcal{C}\boldsymbol{\epsilon}.$$

Matrix $\mathcal{C}$ is positive definite if $\nu \in [0, \frac{1}{2}]$ which can be verified by applying Gershgorin's Theorem. The inverse of $\mathcal{C}$ reads as[1]:

$$\mathcal{C}^{-1} = \frac{1}{E}\begin{bmatrix} 1 & -\nu & -\nu & & & \\ -\nu & 1 & -\nu & & 0 & \\ -\nu & -\nu & 1 & & & \\ & & & 1+\nu & & \\ & 0 & & & 1+\nu & \\ & & & & & 1+\nu \end{bmatrix}. \tag{2.15}$$

Combining all these, we obtain the mixed approach of the elasticity equation by

$$\begin{cases} \nabla \cdot \boldsymbol{\sigma}(\boldsymbol{u}) = -\boldsymbol{F}\delta(\boldsymbol{x}-\boldsymbol{x_0}) & \text{in } \Omega \\ \boldsymbol{\sigma} = \mathcal{C}\boldsymbol{\epsilon} & \text{in } \Omega \\ \boldsymbol{\sigma}\cdot\boldsymbol{n} + \kappa\hat{\boldsymbol{u}} = \boldsymbol{0} & \text{on } \partial\Omega \end{cases} \tag{2.16}$$

The weak form for the general equation is

Find $(\boldsymbol{\sigma}, \boldsymbol{u}) \in W(\Omega) \times V(\Omega)$, such that

$$\int_\Omega \mathcal{C}^{-1}\boldsymbol{\sigma}(\boldsymbol{u})\underline{\underline{\tau}} - \boldsymbol{\epsilon}(\boldsymbol{u})\underline{\underline{\tau}} d\Omega = 0,$$

$$\int_\Omega \boldsymbol{\sigma}(\boldsymbol{u})\nabla\boldsymbol{\phi} d\Omega + \int_{\partial\Omega} \boldsymbol{\sigma}(\boldsymbol{u})\cdot\boldsymbol{n}\boldsymbol{\phi} d\Gamma = \int_\Omega \boldsymbol{F}\delta(\boldsymbol{x})\boldsymbol{\phi} d\Omega,$$
$$\forall(\underline{\underline{\tau}}, \boldsymbol{\phi}) \in W(\Omega) \times V(\Omega).$$

2.3 The Hole Approach in $\mathbb{R}^2$

Since the force is actually applied on a continuous curve, rather than on the complete computational domain, we remove the region occupied by the cell. Then the force on the cell boundary is modelled by boundary condition. Therefore, compared to the previous approach, the new computational domain has a hole inside on whose boundary the forces by the cells are exerted. Therewith, we have boundary conditions on the external boundary, as well as a force boundary condition on the boundary of the cell. The boundary value problem we are working on becomes

$$\begin{cases} -\nabla\cdot\underline{\underline{\sigma}} = 0, & \text{in } \Omega\backslash\Omega_C, \\ \underline{\underline{\sigma}}\cdot\boldsymbol{n} = P(\boldsymbol{x},t)\boldsymbol{n}(\boldsymbol{x}), & \text{on } \partial\Omega_C, \\ \underline{\underline{\sigma}}\cdot\boldsymbol{n} + \kappa\boldsymbol{u} = \boldsymbol{0}, & \text{on } \partial\Omega, \end{cases} \tag{2.17}$$

where Ω is the complete computational domain including the cell and extracellular regions, Ω_C is the region occupied by the cell, and $\partial\Omega_C$ is the boundary of the cell. The corresponding weak form for Eq (2.17) is

$$(WF_{\mathrm{H}}) \begin{cases} \text{Find } \boldsymbol{u} \in H^1(\Omega\backslash\Omega_C), \text{ such that} \\ \int_{\partial\Omega} \kappa\boldsymbol{u}\boldsymbol{\phi} d\Gamma + \int_{\Omega\backslash\Omega_C} \underline{\underline{\sigma}} : \nabla\boldsymbol{\phi} d\Omega = \int_{\partial\Omega_C} P(\boldsymbol{x},t)\boldsymbol{n}(\boldsymbol{x})\boldsymbol{\phi} d\Gamma, \\ \text{for all } \boldsymbol{\phi} \in H^1(\Omega\backslash\Omega_C). \end{cases}$$

Proposition 2.1. *Let $\boldsymbol{u_H}$ and $\boldsymbol{u_I}$, respectively, be solutions to the 'hole-approach', see Equation (2.17) and to the immersed boundary approach, see Equation (2.5). Let $\partial\Omega_C$ denote the line over which internal forces are exerted, and let $\partial\Omega$ be the outer boundary of Ω. Then*

$$\int_{\partial\Omega} \kappa\boldsymbol{u_H} d\Gamma = \int_{\partial\Omega} \kappa\boldsymbol{u_I} d\Gamma = \int_{\partial\Omega_C} P(\mathbf{x},t)\mathbf{n}(\mathbf{x}) d\Gamma$$

.

Proof. To prove that the above equation holds true, we integrate the PDE of both approaches over the computational domain Ω.

For the immersed boundary approach, we get

$$-\int_\Omega \nabla\cdot\underline{\underline{\sigma}} d\Omega = \int_\Omega \sum_{j=1}^{N_S^i} P(\boldsymbol{x},t)\boldsymbol{n}(\boldsymbol{x})\delta(\boldsymbol{x} - \boldsymbol{x}_j^i(t))\Delta\Gamma^{i,j} d\Omega,$$

then after applying Gauss Theorem in the LHS and simplifying the RHS, we obtain

$$-\int_{\partial\Omega} \underline{\underline{\sigma}}\cdot\boldsymbol{n}(\boldsymbol{x}) d\Gamma = \sum_{j=1}^{N_S^i} P(\boldsymbol{x}_j^i(t),t)\boldsymbol{n}(\boldsymbol{x}_j^i(t))\Delta\Gamma^{i,j}.$$

By substituting the Robin's boundary condition and letting $N_S^i \to \infty$, i.e. $\Delta\Gamma^{i,j} \to 0$, the equation becomes

$$\int_{\partial\Omega} \kappa \boldsymbol{u_I} d\Gamma = \int_{\partial\Omega_C} P(\boldsymbol{x}, t)\boldsymbol{n}(\boldsymbol{x}) d\Gamma. \tag{2.18}$$

Subsequently, we do the same thing for the hole approach. Then, we get

$$-\int_{\Omega} \nabla \cdot \underline{\underline{\sigma}} d\Omega = 0,$$

and we apply Gauss Theorem:

$$-\int_{\partial\Omega\cup\partial\Omega_C} \underline{\underline{\sigma}} \cdot \boldsymbol{n}(\boldsymbol{x}) d\Gamma = 0,$$

which implies

$$-\int_{\partial\Omega} \underline{\underline{\sigma}} \cdot \boldsymbol{n}(\boldsymbol{x}) d\Gamma - \int_{\partial\Omega_C} \underline{\underline{\sigma}} \cdot \boldsymbol{n}(\boldsymbol{x}) d\Gamma = 0.$$

Using the boundary conditions, we get

$$\int_{\partial\Omega} \kappa \boldsymbol{u_H} d\Gamma = \int_{\partial\Omega_C} P(\boldsymbol{x}, t)\boldsymbol{n}(\boldsymbol{x}) d\Gamma,$$

which is exactly the same as Eq (2.18). Hence we proved that

$$\int_{\partial\Omega} \kappa \boldsymbol{u_H} d\Gamma = \int_{\partial\Omega} \kappa \boldsymbol{u_I} d\Gamma = \int_{\partial\Omega_C} P(\mathbf{x}, t)\mathbf{n}(\mathbf{x}) d\Gamma.$$

□

Hence, the two different approaches are consistent in the sense of global conservation of momentum and therefore the results from both approaches should be comparable. The only difference between the two approaches is that the hole approach does not consider the stiffness of the cell, since the cell is treated as a hole in the domain. The immerse boundary method contains the internal stiffness of the cell. Therewith, if the cell stiffness is sent to zero, the two formalisms should deliver the same results. Hereby, we are going to prove it mathematically and numerical computations indeed confirm this behaviour.

Therefore, we prove the following proposition:

Proposition 2.2. *For sufficiently smooth solutions, the immersed boundary approach, see Equation (2.5), and the hole approach, see Equation (2.17), yield the same results upon using the following stiffness for the immersed boundary approach*

$$E(\boldsymbol{x}) = \begin{cases} E, & \boldsymbol{x} \in \Omega \backslash \Omega_C, \\ 0, & \boldsymbol{x} \in \Omega_C, \end{cases} \tag{2.19}$$

where E is a constant, Ω_C is the cell region and $\Omega\backslash\Omega_C$ is the extracellular region and Ω_C is surrounded by Ω.

Proof. At this stage we assume that the solution to the immersed boundary approach satisfies a certain regularity such that the L^2-norm of the gradient of the solution is defined. Due to the symmetry of the tensor $\underline{\underline{\epsilon}}(\boldsymbol{u})$, $\forall \boldsymbol{u}$, it follows

$$\int_{\Omega} \underline{\underline{\sigma}} : \nabla \boldsymbol{u} d\Omega = \int_{\Omega} \underline{\underline{\sigma}} : \underline{\underline{\epsilon}}(\boldsymbol{u}) d\Omega.$$

Hence, rewriting the weak form of the immersed boundary approach taking $N_S^i \to \infty$, i.e. $\Delta\Gamma^{i,j} \to 0$, (WF_I) becomes

$$\begin{cases} \text{Find } \boldsymbol{u}, \text{ such that} \\ \displaystyle\int_{\partial\Omega} \kappa \boldsymbol{u}\boldsymbol{\phi} d\Gamma + \int_{\Omega} \underline{\underline{\sigma}} : \underline{\underline{\epsilon}}(\boldsymbol{\phi}) d\Omega = \int_{\partial\Omega_C} P(\boldsymbol{x})\boldsymbol{n}(\boldsymbol{x})\boldsymbol{\phi}(\boldsymbol{x}) d\Gamma, \\ \text{for all } \boldsymbol{\phi}. \end{cases}$$

According to the definition of $\underline{\underline{\sigma}}$ and in Equation (2.19), $\underline{\underline{\sigma}}$ is linearly related to $E(\boldsymbol{x})$. Hence we can reshape the expression for the stiffness as follows

$$E(\boldsymbol{x}) = \begin{cases} E, & \boldsymbol{x} \in \Omega \backslash \Omega_C, \\ \alpha E, & \boldsymbol{x} \in \Omega_C, \end{cases} \tag{2.20}$$

where α is a non-negative constant. Substituting Eq (2.20) into the weak form above, $\int_\Omega \underline{\underline{\sigma}}(\boldsymbol{u}) : \underline{\underline{\epsilon}}(\boldsymbol{\phi}) d\Omega$ splits to $\int_{\Omega\backslash\Omega_C} \underline{\underline{\sigma}}(\boldsymbol{u}) : \underline{\underline{\epsilon}}(\boldsymbol{\phi}) d\Omega + \alpha \int_{\Omega_C} \underline{\underline{\sigma}}(\boldsymbol{u}) : \underline{\underline{\epsilon}}(\boldsymbol{\phi}) d\Omega$. Further, the weak form for the immersed boundary approach, denoted by (WF_I') is given by:

$$(WF_I') \begin{cases} \text{Find } \boldsymbol{u}, \text{ such that} \\ \displaystyle\int_{\partial\Omega} \kappa \boldsymbol{u}\boldsymbol{\phi} d\Gamma + \int_{\Omega\backslash\Omega_C} \underline{\underline{\sigma}}(\boldsymbol{u}) : \underline{\underline{\epsilon}}(\boldsymbol{\phi}) d\Omega + \alpha \int_{\Omega_C} \underline{\underline{\sigma}}(\boldsymbol{u}) : \underline{\underline{\epsilon}}(\boldsymbol{\phi}) d\Omega = \int_{\partial\Omega_C} P(\boldsymbol{x})\boldsymbol{n}(\boldsymbol{x})\boldsymbol{\phi}(\boldsymbol{x}) d\Gamma, \\ \text{for all } \boldsymbol{\phi}. \end{cases}$$

Recalling the weak form of the hole approach:

$$(WF_{\mathrm{H}}) \begin{cases} \text{Find } \boldsymbol{u} \in H^1(\Omega\backslash\Omega_C), \text{ such that} \\ \displaystyle\int_{\partial\Omega} \kappa \boldsymbol{u}\boldsymbol{\phi} d\Gamma + \int_{\Omega\backslash\Omega_C} \underline{\underline{\sigma}}(\boldsymbol{u}) : \underline{\underline{\epsilon}}(\boldsymbol{\phi}) d\Omega = \int_{\partial\Omega_C} P(\boldsymbol{x}, t)\boldsymbol{n}(\boldsymbol{x})\boldsymbol{\phi} d\Gamma, \\ \text{for all } \boldsymbol{\phi} \in H^1(\Omega\backslash\Omega_C). \end{cases}$$

Since we want to prove the consistency of these two approaches, we rewrite $\boldsymbol{u}$ in (WF_I') into $\boldsymbol{u_1}$ and $\boldsymbol{u_2}$ in (WF_H). Denoting $\boldsymbol{v} = \boldsymbol{u_1} - \boldsymbol{u_2}$ and subtracting the equations in both weak forms, using linearity the weak form for $\boldsymbol{v}$ is

$$(WF_{\mathrm{v}}) \begin{cases} \text{Find } \boldsymbol{v}, \text{ such that} \\ \displaystyle\int_{\Omega\backslash\Omega_C} \underline{\underline{\sigma}}(\boldsymbol{v}) : \nabla\boldsymbol{\phi} d\Omega + \int_{\partial\Omega} \kappa \boldsymbol{v}\boldsymbol{\phi} d\Gamma = -\alpha \int_{\Omega_C} \underline{\underline{\sigma}}(\boldsymbol{u_1}) : \underline{\underline{\epsilon}}(\boldsymbol{\phi}) d\Omega \\ \text{for all } \boldsymbol{\phi} \text{ and } \alpha \geqslant 0. \end{cases}$$

Since $\boldsymbol{\phi}$ is a test function, which we can choose freely provided the integrals make sense, we choose $\boldsymbol{\phi} = \boldsymbol{v}$. The equation in weak form (WF_v) becomes

$$\begin{aligned} \int_{\Omega\backslash\Omega_C} \underline{\underline{\sigma}}(\boldsymbol{v}) : \underline{\underline{\epsilon}}(\boldsymbol{v}) d\Omega + \int_{\partial\Omega} \kappa \|\boldsymbol{v}\|^2 d\Gamma &= \alpha \| \int_{\Omega_C} \underline{\underline{\sigma}}(\boldsymbol{u_1}) : \underline{\underline{\epsilon}}(\boldsymbol{v}) d\Omega \| \\ \text{(Cauchy-Schwartz Inequality)} &\leqslant \alpha (\int_{\Omega_C} \|\underline{\underline{\sigma}}(\boldsymbol{u_1})\|^2 d\Omega)^{1/2} (\int_{\Omega_C} \|\underline{\underline{\epsilon}}(\boldsymbol{v})\|^2 d\Omega)^{1/2} \\ \text{(Continuity/Boundedness, } \exists K > 0) &\leqslant \alpha K (\int_{\Omega_C} \|\nabla \boldsymbol{u_1}\|^2 d\Omega)^{1/2} (\int_{\Omega_C} \|\nabla \boldsymbol{v}\|^2 d\Omega)^{1/2}. \end{aligned}$$

Note $\int_{\Omega\backslash\Omega_C} \underline{\underline{\sigma}}(\boldsymbol{v}) : \underline{\underline{\epsilon}}(\boldsymbol{v}) d\Omega$ and $\int_{\partial\Omega} \kappa \boldsymbol{v}^2 d\Gamma$ are always non-negative with $\kappa > 0$.

By coercivity (note that Korn's inequality holds), there exists a positive constant β, such that

$$\int_{\Omega\backslash\Omega_C} \underline{\underline{\sigma}}(\boldsymbol{v}) : \underline{\underline{\epsilon}}(\boldsymbol{v}) d\Omega \geqslant \beta \int_{\Omega\backslash\Omega_C} \|\nabla \boldsymbol{v}\|^2 d\Omega, \quad \forall \boldsymbol{v}.$$

Note that the domains for the solution in the immersed boundary approach and the hole approach are not the same, and in (WF_v) $\boldsymbol{\phi}$ and $\boldsymbol{v}$ are defined in $\Omega\backslash\Omega_C$. We consider continuous of $\boldsymbol{\phi}$ and $\boldsymbol{v}$ over Ω. Summarizing all the inequalities above, the following sequential inequality is developed:

$$\begin{aligned} 0 \leqslant \beta \int_{\Omega\backslash\Omega_C} \|\nabla \boldsymbol{v}\|^2 d\Omega &\leqslant \int_{\Omega\backslash\Omega_C} \underline{\underline{\sigma}}(\boldsymbol{v}) : \underline{\underline{\epsilon}}(\boldsymbol{v}) d\Omega \leqslant \int_{\Omega\backslash\Omega_C} \underline{\underline{\sigma}}(\boldsymbol{v}) : \underline{\underline{\epsilon}}(\boldsymbol{v}) d\Omega + \int_{\partial\Omega} \kappa \boldsymbol{v}^2 d\Gamma \\ &= \alpha \| \int_{\Omega_C} \underline{\underline{\sigma}}(\boldsymbol{u_1}) : \underline{\underline{\epsilon}}(\boldsymbol{v}) d\Omega \| \leqslant \alpha K (\int_{\Omega_C} \|(\nabla \boldsymbol{u_1}\|^2 d\Omega)^{1/2} (\int_{\Omega_C} \|\nabla \boldsymbol{v}\|^2 d\Omega)^{1/2}. \end{aligned}$$

Applying the equation for the stiffness in Eq (2.19), i.e. $\alpha \to 0$, it can be concluded that

$$\begin{aligned} & 0 \leqslant \beta \int_{\Omega\backslash\Omega_C} \|\nabla \boldsymbol{v}\|^2 d\Omega \leqslant 0, \quad \text{for } \beta > 0 \\ & \Rightarrow \int_{\Omega\backslash\Omega_C} \|\nabla \boldsymbol{v}\|^2 d\Omega = 0 \\ & \Rightarrow \nabla \boldsymbol{v} = \boldsymbol{0}, \quad \text{in } \Omega\backslash\Omega_C. \end{aligned}$$

This implies that v is constant over $\Omega \setminus \Omega_C$. On the other hand, if the internal integral is removed, then the inequality is developed as

$$\begin{aligned} 0 \leqslant \int_{\partial\Omega} \kappa \boldsymbol{v}^2 d\Omega \leqslant \int_{\Omega\backslash\Omega_C} \underline{\underline{\sigma}}(\boldsymbol{v}) : \underline{\underline{\epsilon}}(\boldsymbol{v}) d\Omega + \int_{\partial\Omega} \kappa \boldsymbol{v}^2 d\Gamma &= \alpha \| \int_{\Omega_C} \underline{\underline{\sigma}}(\boldsymbol{u_1}) : \underline{\underline{\epsilon}}(\boldsymbol{v}) d\Omega \| \\ &\leqslant \alpha K (\int_{\Omega_C} \|(\nabla \boldsymbol{u_1}\|^2 d\Omega)^{1/2} (\int_{\Omega_C} \|\nabla \boldsymbol{v}\|^2 d\Omega)^{1/2}. \end{aligned}$$

Using $\boldsymbol{u_1}$, $\boldsymbol{v}$, it follows that as $\alpha \to 0$, then $\boldsymbol{v} = \boldsymbol{0}$ on $\partial\Omega$. Combined with the equation stating $\nabla \boldsymbol{v} = \boldsymbol{0}$ in $\Omega\backslash\Omega_C$, it can be concluded that

$$\boldsymbol{v} = \boldsymbol{0}, \quad \text{in } \Omega\backslash\Omega_C,$$

with the condition of stiffness in Equation (2.19). Hence, we have proved $\boldsymbol{u_1} = \boldsymbol{u_2}$ in $\Omega\backslash\Omega_C$ in the limit of $\alpha \to 0$, which verified the consistency of the solutions to these two approaches. □

2.4 Small Cell Approach

If we consider a domain in which many cells are moving and exerting forces, then the aforementioned two approaches will be very extensive from a computational point of view. Therefore, we will simplify the cell boundary to a low-order polygon, such as to a triangle or square. Furthermore, if the cell size is smaller than the mesh size, then we cannot break the cell boundary into finite segments by the mesh for both approaches.

Inspired by finite boundary segments which actually build up a polygon, we can simulate the circular cell by different kinds of polygons.

Eq (2.5) is still used as the basis for the computation of the forces that are exerted by the cells. However, we study the use of just a few boundary segments per cell in such a way that the total force exerted by the cell is the same regardless the order of the polygon.

2.5 Approaches to Calculate Near-Cell Region Area

The cells exert forces on their immediate environment and hence all the points of the computational domain will be displaced. The displacement vector will induce a contraction of the near cell region. This contraction is quantified by the area of the near-cell region. Generally speaking, we compute the area by using the new positions of the nodal points of the mesh, which can be expressed in three ways: one is the direct approach by summing up all the mesh triangles area after displacement which we denote by A_P:

$$A_P := A_\Omega = \sum_{k=1}^{n_{el}} A_{e_k} = \sum_{k=1}^{n_{el}} \frac{\|\Delta e_k\|}{2} \tag{2.21}$$

where

$$\|\Delta e_k\| = \det \begin{Vmatrix} 1 & x_{k_1} & y_{k_1} \\ 1 & x_{k_2} & y_{k_2} \\ 1 & x_{k_3} & y_{k_3} \end{Vmatrix} \tag{2.22}$$

for each element e_k. An alternative procedure relies on the use of the integral of the gradient tensor of the displacement over the computational domain. According to Lubliner [7], for each nodal point, the new position is

$$\boldsymbol{x}(t) = \boldsymbol{X} + \boldsymbol{u}(\boldsymbol{x}),$$

where $\boldsymbol{X}$ stands for the initial position and $\boldsymbol{x}(t)$ is the position at time t. Defining the gradient matrix of displacement $\boldsymbol{J} = \nabla_{\boldsymbol{X}} \boldsymbol{u}$, the matrix notation can be worked out as

$$d\boldsymbol{x} = \frac{\partial \boldsymbol{x}}{\partial \boldsymbol{X}} d\boldsymbol{X} = (\boldsymbol{I} + \nabla_{\boldsymbol{X}} \boldsymbol{u}) d\boldsymbol{X} = (\boldsymbol{I} + \boldsymbol{J}) d\boldsymbol{X}, \tag{2.23}$$

where $\dfrac{\partial \boldsymbol{x}}{\partial \boldsymbol{X}} d\boldsymbol{X}$ is the Jacobian matrix. The volume can be calculated by:

$$d\boldsymbol{x} = \det(\boldsymbol{I} + \boldsymbol{J}) d\boldsymbol{X}, \tag{2.24}$$

that is, theoretically

$$A_\Omega = \int_{\Omega_0} \det(\boldsymbol{I} + \boldsymbol{J}) d\boldsymbol{X}, \tag{2.25}$$

where Ω_0 is the initial domain and by the use of the Newton-Côtes quadrature Rule one gets

$$A_\Omega \approx A_{NC} = \frac{\|\Delta e_k\|}{6} \sum_{k=1}^{n_{el}} \sum_{i=1}^{3} \det(\boldsymbol{I} + \boldsymbol{J}(\boldsymbol{x_{k_i}})), \tag{2.26}$$

over all triangular elements of the mesh, and we denote this by A_{NC}. Another possibility to compute the area of Ω is based on connecting all the nodal points on the boundary to build up a polygon. Then this polygon area is an approximation of the deformed area. To calculate the polygon area, one can use shoelace method derived by Meister [8] in 1769. Suppose we have a polygon with n vertices, then the area is calculated by

$$A_\Omega \approx A_{SL} = \frac{1}{2} \| \sum_{i=1}^{n} (x_i y_{i+1} - x_{i+1} y_i) \|, \tag{2.27}$$

where (x_i, y_i), $i = 1, \ldots, n$ is the coordinate of vertex i and $(x_{n+1}, y_{n+1}) = (x_1, y_1)$. Note that the vertices should be sorted in counter clockwise or clockwise direction.

To have a better insight of how these different computational approaches affect the cell and the near-cell region, we calculate the reduction of the area with respect to the initial area. If we denote the area after deformation by A_Ω and the original area is A^0_Ω, then the ratio is calculated by

$$r = \frac{\|A_\Omega - A^0_\Omega\|}{A^0_\Omega}. \tag{2.28}$$

3 Numerical Results for the Point Source Approaches

This section describes the numerical approximation of the solution with a point source. The various methodologies from the previous section will be analyzed using computational examples.

If the dimensionality exceeds one, then the Green's function for the unbounded domain is not in $H^1(\Omega)$. This is the main reason why we analyze the convergence behaviour of the numerical approximations that have been obtained by the use of earlier mentioned methods. We consider the L^2 norm which is defined by $\|\boldsymbol{u}\|_{L^2(\Omega)} = (\int_\Omega \|\boldsymbol{u}^2\| d\Omega)^{1/2}$. To compute the convergence rate, we use the expression:

$$2^p = \frac{\|u_h\|_{L^2(\Omega)} - \|u_{h/2}\|_{L^2(\Omega)}}{\|u_{h/2}\|_{L^2(\Omega)} - \|u_{h/4}\|_{L^2(\Omega)}}. \tag{3.1}$$

where h represents the mesh size, and u_h represents the numerical approximation obtained by using a mesh with mesh size h.

In the two-dimensional case, we investigate the direct approach and the mixed finite element method for the case of presence of one point force. The two methods show consistency, as can be seen from Figure 3.1 and the results have been presented in Table 3.1. It can be seen that there is small difference between the results from the two methods. However, the order of convergence, p, is comparable. This simulation is repeated in the three-dimensional case.

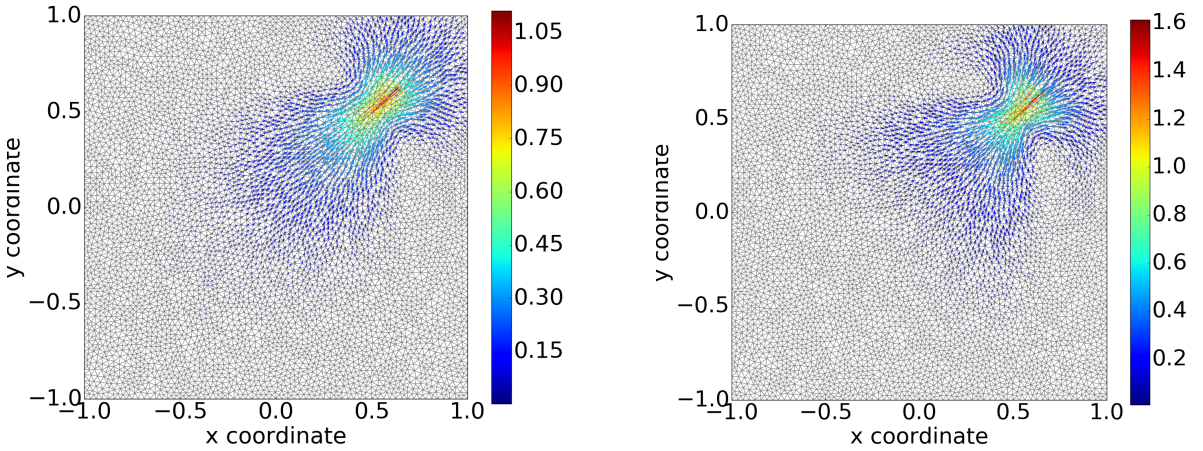

(a) The Direct approach

(b) The Mixed approach

Figure 3.1: With only one point source in the unit cube box, three figures show the displacement results of elasticity equation expressed in Eq (2.10) with applying two approaches respectively.

Subsequently we compare the results from the three methods in the three-dimensional case. For the homogenization approach, we have used $\gamma = 10^{-4}$. The plots in Figure 3.2 indicate consistency between the results from the direct and mixed finite element method. However, due to the choice of γ, it can be seen that there is a discrepancy with the results from the homogenization approach.

We show the L_2-norms of the displacement for different mesh sizes using the three methods in Table 3.2. The computation times for the homogenization and mixed finite element method were large. It is also seen that the homogenization approach gives the worst convergence behaviour. This may be attributed to the current choice of γ. For the mixed and direct approaches, the convergence rates for the L_2-norm of the displacement are comparable. There is also difference between the norms of the mixed and direct approach. Further mesh refinement could not be carried out due to memory limitations.

Table 3.1: The norm and the convergence order of different variables by two approaches, which are used to solve elasticity equation with only one point source in two dimensions

(a) The L_2-norm of displacement $\boldsymbol{u}$

Mesh size	**Direct approach**	**Mixed approach**
h	0.24970447276635543	0.25945988770849937
h/2	0.26018316808001607	0.2638741301913874
h/4	0.2635212165031773	0.26494097303479763
p	1.650382312	2.048779918

(b) The strain energy density $M(\boldsymbol{u}) = \int_\Omega 1/2 \times \underline{\underline{\sigma}}(\boldsymbol{u}) : \underline{\underline{\epsilon}}(\boldsymbol{u}) d\Omega$

Mesh size	**Direct approach**	**Mixed approach**
h	0.4103502667213455	0.5043228278539474
h/2	0.5941144806691983	0.7077592679206937
h/4	0.7373671562791781	0.8398165200852681
p	0.3592937598	0.6234145897

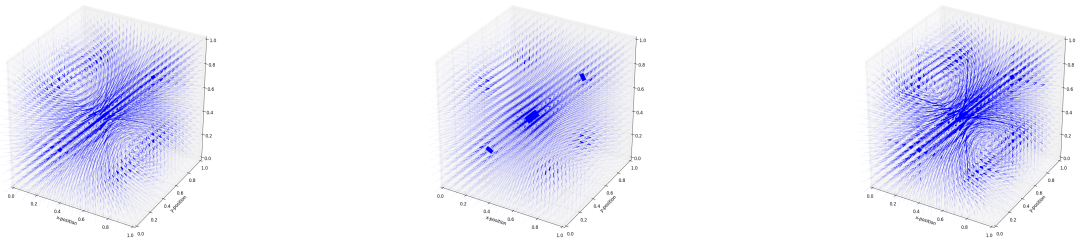

(a) Direct approach (b) Homogenization approach (c) Mixed approach

Figure 3.2: With only one point source in the unit cube box, three figures show the displacement results of elasticity equation expressed in Eq (2.10) with applying three approaches respectively.

Table 3.2: The L_2-norm of the solution to the elasticity equation (i.e. displacement) by different approaches which are used to solve elasticity equation with only one point source in three dimensions

Mesh size	**Direct approach**	**Homogenization approach**	**Mixed approach**
h	0.30538580699248863	1.6490699243682738	0.3892974553769718
h/2	0.39203123028339903	0.8684113851504227	0.5365958803544032
h/4	0.4159570965258156	0.39920401984082754	0.5793804169589923
p	1.856552388	0.7344659892	1.783580634

4 Applications in Wound Healing Process

Dermal wounds may lead to various pathological problems, therefore it is vital for the skin to have a fast and effective healing for the wounds.

After the inflammatory phase, fibroblasts are attracted from the edge of the wound towards the interior of the wound as a result of cytokines secreted by the immune cells[4]. Once they have entered the wound, fibroblasts can differentiate into myofibroblats which pull the extracellular matrix and thereby wound deformation of the near-by tissue is caused[4].

Subsequently, we use the finite element method to analyse the performance of the immerse boundary approach and hole approach. Since we are interested in the behaviour of the solution in the vicinity of the positions where point forces are exerted, we introduce a subdomain near the locations where the point sources are exerted. This near-by subdomain, as well as the entire computational domain and the circular line where the forces are exerted are shown in Figure 4.1. The meshes for the two approaches are the same, except for the use of a 'hole' in the hole-approach. The circular curve where the forces are applied models a cell boundary, with its inner region modelling a myofibroblast that exerts forces on its direct environment.

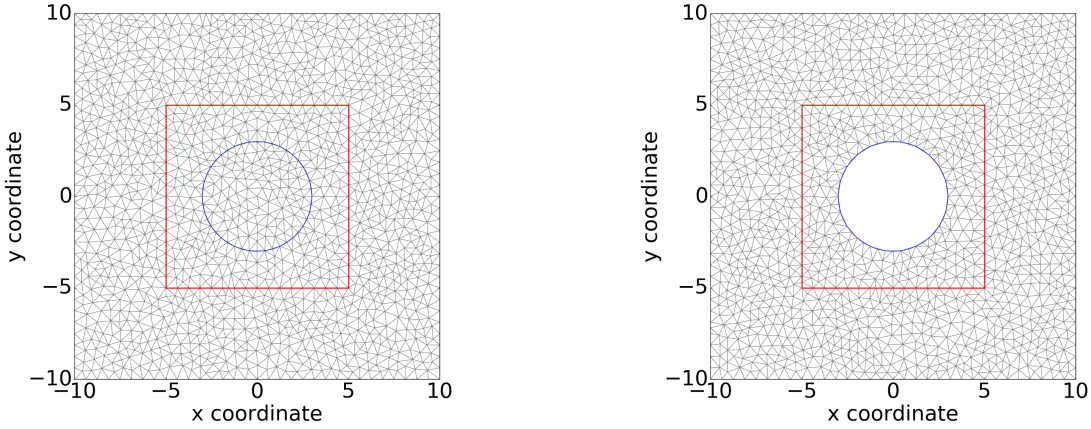

(a) The immersed boundary approach

(b) The hole approach

Figure 4.1: Two subplots show the mesh used for the immersed boundary approach and hole approach. We use $(-10, 10) \times (-10, 10)$ ***as computational domain,*** $(-5, 5) \times (-5, 5)$ ***as near-cell region domain of which the boundary is marked with red lines and the cell is drawn in blue.***

The values of the parameters used in this simulation have been listed in Table 4.1.

Table 4.1: Parameter values

Parameter	Description	Value	Dimension
E	Substrate elasticity	1	$kg/(\mu m \cdot min^2)$
P	Magnitude of the force exerted by the cell	1	$kg \cdot \mu m/min^2$
R	Cell radius	3	μm
κ	Boundary condition coefficient	10	–
ν	Poisson's ratio	0.49	–

4.1 The Immersed Boundary Approach

The boundary of the circle is divided into mesh points, which are connected by line segments. On each midpoint of the line segments, a point force normal to the line segment towards the

centre of the circle is exerted. Figure 4.2 displays the initial cell and the nearby region with is included in the red square, as well as its deformations, which are hard to see due to very small displacements. Both approaches have been considered, see Figure 4.2(a) and 4.2(b). Subsequently we are interested in the area of the cell and the near-by region. We use a direct finite element method and a mixed finite element method to compute the displacement. To compute the area of the circular cell and of the region enclosed by the red curve, we use the methods that have been outlined in Section 2.5. According to Table 4.2(a), all methods to compute the area gave nearly the same result and therefore we have no preference for the method to compute the area. Furthermore, the difference in area between the mixed approach and the direct approach is not very large, however, the difference in computational time is large: the mixed finite element approach takes approximately 12 times as much computation time as the direct method does. This is explained by the fact that there are two variational problems to be solved in the mixed finite element approach instead of only one as in the direct approach. Due to different integrability requirements between the mixed finite element method and the direct finite element method, different finite elements need to be used for these methods, which may cause the discrepancy between the computation times. Regarding the order of accuracy of the strain energy in the near-cell region, the mixed approach gave an order of about 0.6, whereas the direct method gave an order of about 2. Hence the mixed finite element method turned to be performing worse than the direct approach. The values have been detailed in Table 4.2(b).

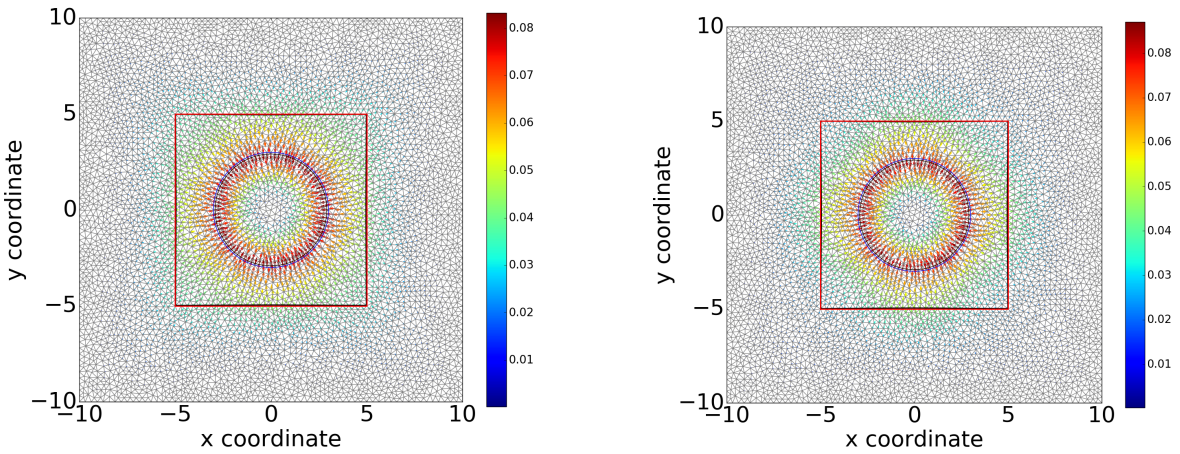

(a) Direct approach

(b) Mixed approach

Figure 4.2: Displacements results of the delta approach when we take the cell as the circular shape with two different approaches. The red square depicts the initial near-cell region and we indicate the deformed near-cell region by black line. Similarly, we also plot the initial and deformed cell in blue and black respectively.

4.2 The Hole Approach

As it can be seen from the mesh in Figure 4.1, the cell region is a hole in the domain and hence it is not part of the computational domain. Therefore, the boundary of the cell is part of the boundary of the computational domain and hence we apply a force boundary condition on it. Analogous to the Delta functions approach, the boundary of the circular is divided into meshpoints and line segments. On each line segment on the cell boundary, a force is applied, see Equation (2.1). In Figure 4.3, one can see that the cell deforms from a circle due to the exerted forces. As the resolution is increased, that is, the boundary of the cell is split into more

Table 4.2: Numerical results for the direct and the mixed approach

(a) The percentage of area reduction of near-cell region and the time cost for direct and mixed approach

	Direct Approach	**Mixed Approach**
$A_{NC}(\%)$	1.41244	1.33568
$A_{SL}(\%)$	1.41468	1.33552
$A_P(\%)$	1.41468	1.33552
Time cost(s)	1.63839	23.16246

(b) Total strain energy in near-cell region $M(\boldsymbol{u}) = \int_{\Omega_{near-cell}} 1/2 \times \underline{\underline{\sigma}}(\boldsymbol{u}) : \underline{\underline{\epsilon}}(\boldsymbol{u}) d\Omega$

Mesh Size	**Direct Approach**	**Mixed Approach**
h	0.731769599864198	0.750236292034798
$h/2$	0.7331815460820671	0.7429632344713815
$h/4$	0.7334801036608783	0.7382916335116566
p	2.24160404	0.6386449478

line segments, the shape of the cell tends closer and closer to the rounded shape; see Figure 4.3.

We compare the results from the immersed boundary approach to the results from the 'hole' approach. From Figure 4.4, it can be seen that there is a large difference between the results from the two approaches. In particular, the magnitude of the displacement from the hole approach is more than 13 times as large as the displacement from the immersed boundary approach. This discrepancy is caused by the interaction with the region inside the circular cell, which is incorporated in the immersed boundary approach and not in the hole approach. Therefore, we adjust the stiffness of the region inside the circular cell to zero, by Equation (2.19). Then we redo the simulation and plot the results in Figure 4.5. The results of area and total strain energy density in near-cell region have been documented in Table 4.4, and as a result of the use of equation (2.19), it can be seen that the hole approach and immersed boundary approach are consistent. Further, it can be observed that the order of accuracy of the hole approach is slightly better, whereas the adjusted immersed boundary approach is about a factor four more economical from a computational efficiency point of view.

However, rather than setting the stiffness modulus to zero inside the cell, we set the cell stiffness modulus to a small positive constant, so that the numerical results are comparable. Hence, for the implementation, we use

$$E(\boldsymbol{x}) = \begin{cases} E, & \boldsymbol{x} \in \Omega \backslash \Omega_C, \\ \gamma, & \boldsymbol{x} \in \Omega_C, \end{cases} \tag{4.1}$$

where γ is a small positive constant. In the following contents about adjusted immersed boundary approach, γ is 10^{-5} if there is no further declaration. Due to multiple choices of γ, the value of γ determines the accuracy and convergence of the adjusted immersed boundary approach. In this report, γ varies from 10^{-6} to 10^{-3}. A_{SL} is selected to determine the percentage of area reduction. In Table 4.3, besides the area reduction, the convergence rate of the L_2-norm of the solution and the total strain energy density in the near-cell region are shown. It can be concluded that the value of γ does have a modest impact in the current range, and the influences on various categories are distinct. In other words, for the area reduction, it is verified that the smaller value γ is, the closer the result is to the one in hole approach. Nevertheless, there is 'bell shape' behaviour appearing for the convergence rate of $\|\boldsymbol{u}\|_{L_2}$ with decreasing

tendency for the convergence rate of the total strain energy density in the near-cell region as γ is declining.

Table 4.3: Numerical results of adjusted immersed boundary approach and hole approach with multiple choices of γ

Approach	γ	**The Percentage of Area Reduction(%)**	**Convergence Rate of** $\|\boldsymbol{u}\|_{L_2}$	**Convergence Rate of** $\int_{\Omega_{near-cell}} 1/2 \times \underline{\underline{\sigma}}(\boldsymbol{u}) : \underline{\underline{\epsilon}}(\boldsymbol{u}) d\Omega$
Hole Approach	–	17.49741928	1.978019816	2.064701439
Adjusted Immersed Boundary Approach	10^{-3}	17.29570621	1.882445881	1.929776181
	10^{-4}	17.48242014	1.984418004	1.704289701
	10^{-5}	17.49936018	1.984324634	1.706561293
	10^{-6}	17.50084960	1.769210872	1.583005166

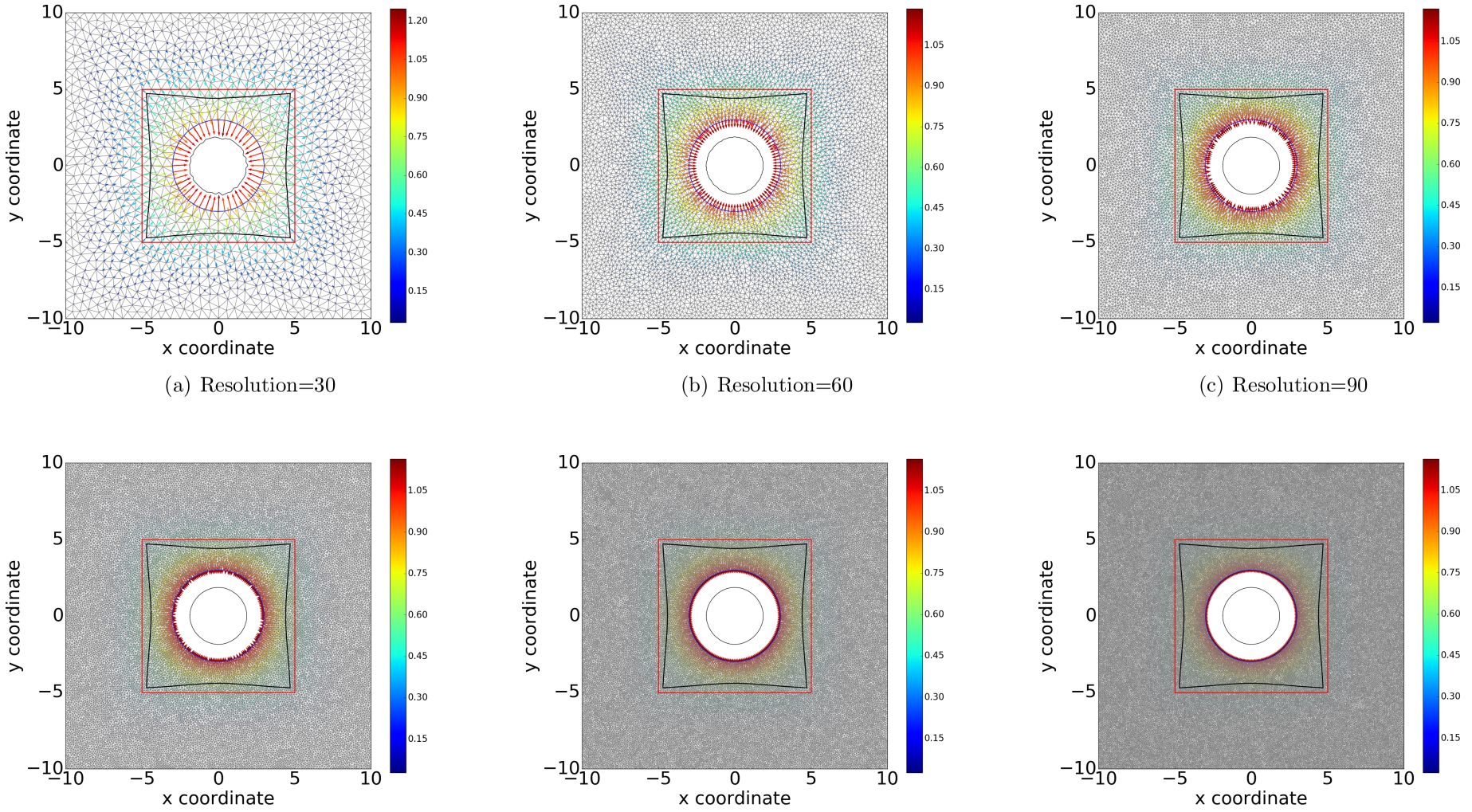

(a) Resolution=30 (b) Resolution=60 (c) Resolution=90

(d) Resolution=120 (e) Resolution=150 (f) Resolution=180

Figure 4.3: *In each subplot, it shows the displacement results of cell using the same size of the cell but with different resolutions. The red square is the initial near-cell region and the black curve shows the deformed near-cell region. The circular shape in the hole depicts the cell shape.*

Table 4.4: Numerical results of adjusted immersed boundary approach and hole approach

(a) The percentage of area change of near-cell region of adjusted immersed boundary approach and hole approach

	Adjusted Immersed Boundary Approach	**Hole Approach**
$A_{NC}(\%)$	17.50153	17.52235
$A_{SL}(\%)$	17.50361	17.49742
$A_P(\%)$	17.50361	17.49742
Time Cost(s)	1.99139	8.71979

(b) Total strain energy in near-cell region $M(\boldsymbol{u}) = \int_{\Omega_{near-cell}} 1/2 \times \underline{\underline{\sigma}}(\boldsymbol{u}) : \underline{\underline{\epsilon}}(\boldsymbol{u}) d\Omega$

Mesh Size	**Adjusted Immersed Boundary Approach**	**Hole Approach**
h	3.365449962383368	3.37260704860696
$h/2$	3.3403267753142813	3.3393598072412605
$h/4$	3.331940166683918	3.3314125274669273
p	1.582860055	2.064701439

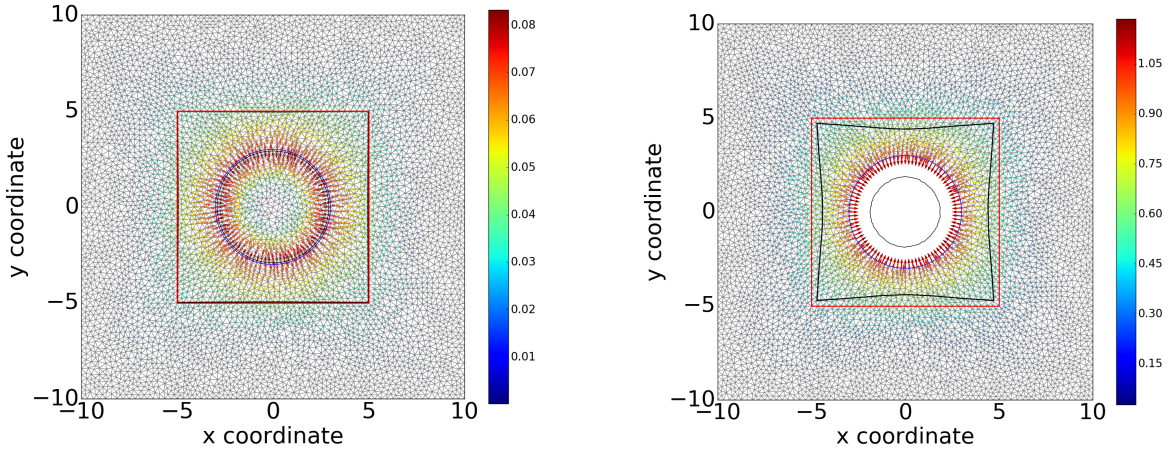

(a) Immersed boundary approach

(b) Hole approach

Figure 4.4: Displacement results of immersed boundary approach (Eq (2.5)) and hole approach (Eq (2.17)) when the same mesh structured used except the hole and the same parameter values applied. The black line shows the deformed cell and near-cell region and the other colour lines represent the original status.

4.3 Small-Cell Approach

In the applications that we study, we are interested in multiple cells that are migrating through the computational domain. In typical situations, the cell size is much smaller than the domain size and the cell size could even be smaller than the element size from the discretization. Therefore, it is expensive from a computational point of view to divide the cell boundary into many meshpoints and line segments in these applications. Hence we are interested in the numerical accuracy if each cell is approximated by a simple polygon like a triangle or square instead of a high order polygon. For now we focus on one cell only, and in the beginning we use a relatively big cell (see Figure 4.6), then we move to the circumstance of multiple small cells and analyse the numerical results as we increase the polygonal order. The parameters values

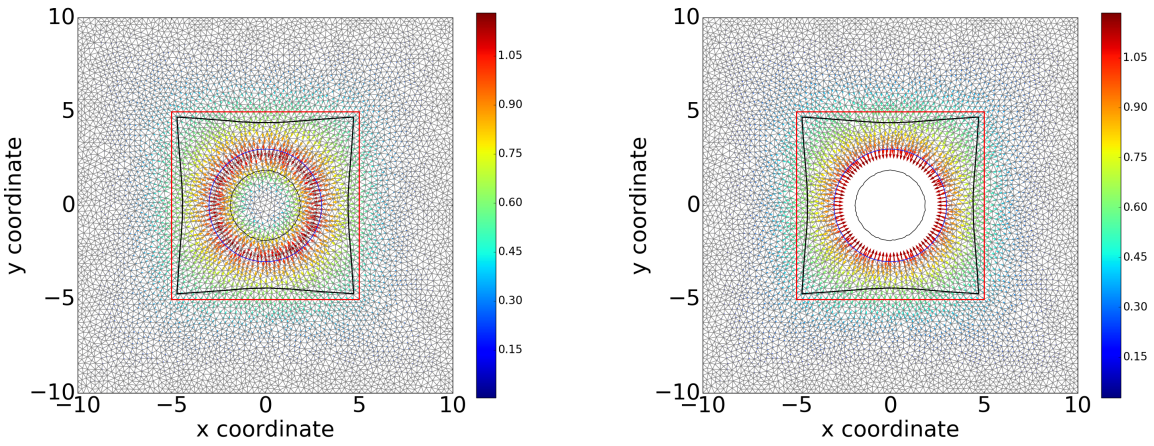

(a) Adjusted immersed boundary approach

(b) Hole approach

Figure 4.5: Displacement results of adjusted immersed boundary approach (Eq (2.5)) and hole approach (Eq (2.17)) when the same mesh structured used except the hole and the same parameter values applied. The black line shows the deformed cell and near-cell region and the other colour lines represent the original status.

are displayed in Table 4.5. In Figure 4.6, once can clearly see how the number of line segments used in the approximation of the cell boundary influences the displacement pattern. From the images it follows that convergence towards a circle is attained as the polygon consists of more line segments.

Table 4.5: Parameter values

Parameter	Description	Value	Dimension
E	Substrate elasticity	1	$kg/(\mu m \cdot min^2)$
P	Magnitude of the force exerted by the cell	10	$kg \cdot \mu m/min^2$
R	Cell radius	0.1	μm
κ	Boundary condition coefficient	10	–
ν	Poisson's ratio	0.49	–
λ	Parameter in Point Poisson Process of cells	15	–

In the multi-cell simulations, we locate the cells according to a Point Poisson Process with rate parameter λ, where we choose $\lambda = 15$ from [6]. The Point Poisson process is applied to a scaled version of the domain of computation. Further the cell radius has been scaled down to 0.1 of the radius in the previous calculations. The cell domain is the same as in the earlier simulations. In order to visualize the deformation of the domain of computation, we set the magnitudes of the forces exerted by the cells to 10. In the simulations, we use the immersed boundary method with low order polygonal approximations of the circular cells. We investigate the performance in terms of the numerical solution with respect to the degree of polygons. The numerical numbers that we investigate are the area reduction due to the pulling forces exerted by the cells and the computation time. In all the calculations where we vary the degree of the polygonal approximation of the cells, we use the same number of cells and the same positions of the centres of the cells. Upon increasing the degree of the polygon, one gradually converges to a circle as can be observed from Figure 4.6. In the current computations we use a maximum number of eight nodes on the cells, that is, we use octagons as the highest polygonal order. The smallest order of polygonal approximation is the triangular shape. Lower order of polygonal

approximation admits the advantage that computation times can be reduced due to a lower number of function evaluations from point forces. In the computations, it has turned out that the use of triangles gave a reduction of computation time of roughly fifty percent with respect to the octagonal representation of the cell boundaries.

An example of a simulation is shown in Figure 4.7, where multiple cells are shown as circles, and the contraction of the region is shown. The cell size is smaller than the mesh size, so we applied the small cell approach here to investigate the area reduction of the region. We selected the polygons such that the area of each cell is equal in all simulation runs as well as the centres of the cells. Figure 4.8 displays the computation time and relative reduction of area as a function of polygonal degree. It can be seen that a square representation of the circles already reproduces the results of the octagonal representation very well. Since the computational time is much smaller than the computation time for the octagonal representation, we recommend to approximate the cell boundary by a square if a large number of small cells are used.

To determine the time cost of each area determination method, we show the computational times in Table 4.6. The computational times increase very little with the polynomial degree. Further, the results indicate that the procedure to get A_{SL} from Equation (2.27) is the most efficient method. Computation times are about two percent of the computation times using the other methods.

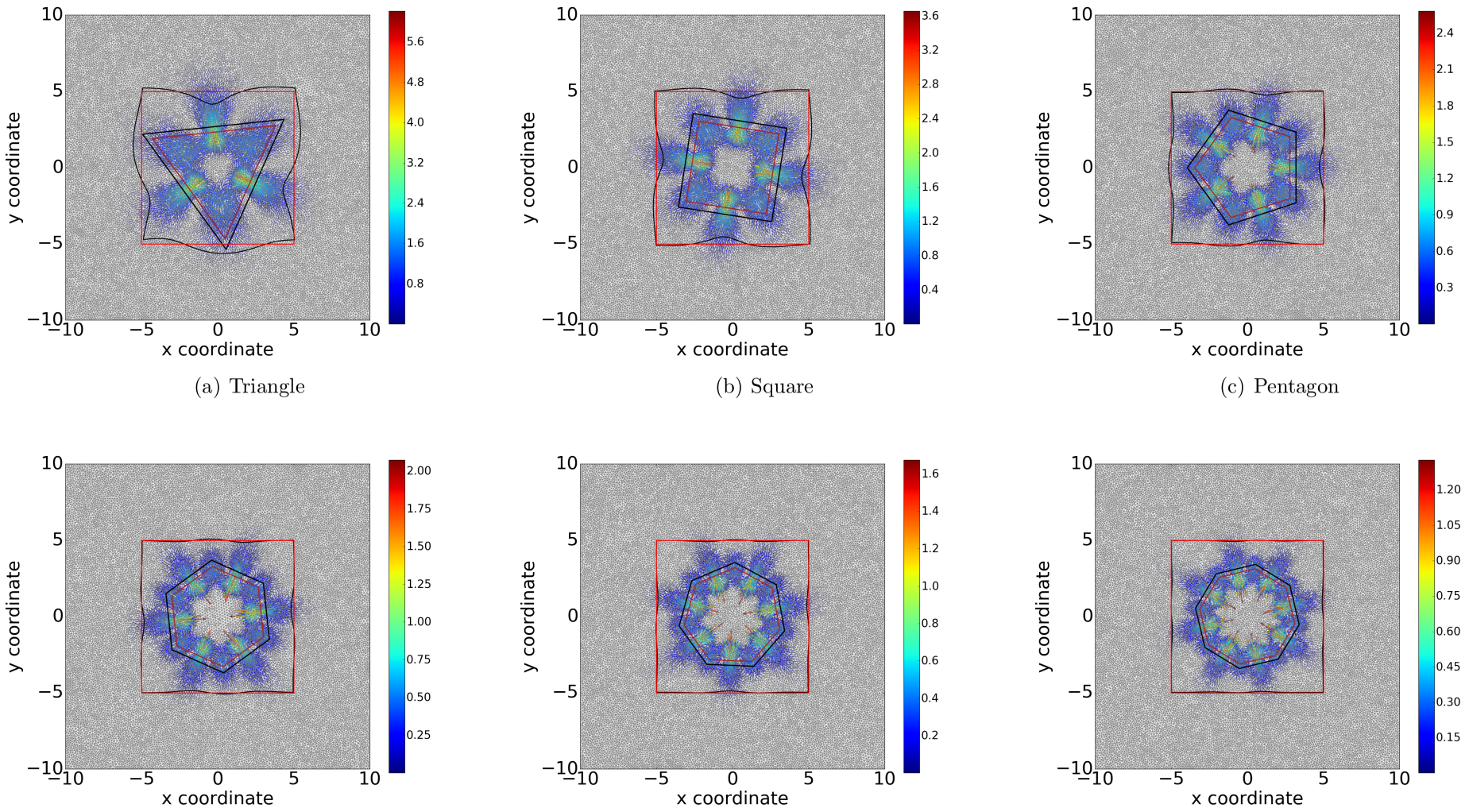

(a) Triangle (b) Square (c) Pentagon

(d) Hexagon (e) Heptagon (f) Octagon

***Figure 4.6:** In each subplot, it shows the displacement results of cell using the same size of the cell but with different resolutions. The red square is the initial near-cell region and the black curve shows the deformed near-cell region. The circular shape in the hole depicts the cell shape.*

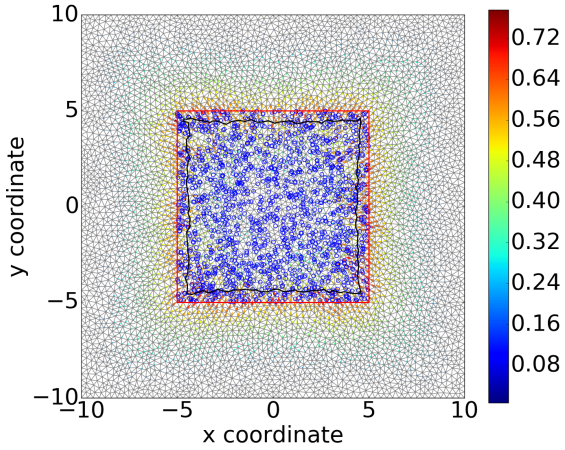

***Figure 4.7:** Equal-area square is used to approximate all cells. The blue circles are the cell positions, the red line and black curve present the original and deformed boundary of the region.*

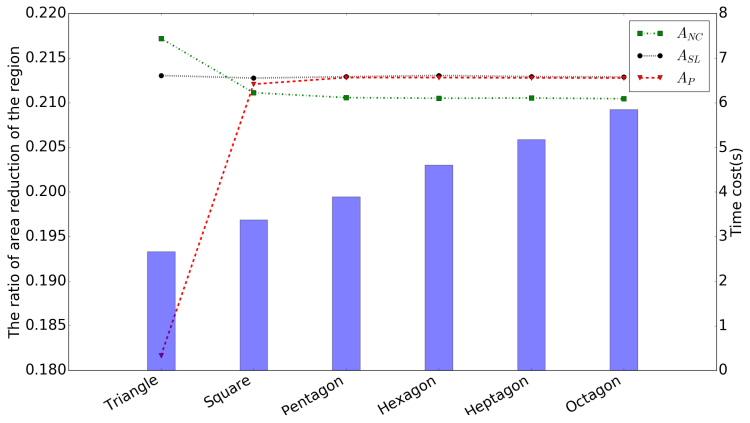

***Figure 4.8:** The blue bars indicate the computational cost; the curves display the relative reduction of area.*

5 Conclusion

In this paper, we mainly discussed different approaches to solve linear elasticity problems with point sources. The homogenization approach and the mixed approach do not seem to significantly improve the numerical accuracy if the displacement and area is to be determined.

In order to simulate wound contraction, it is crucially important to solve the elasticity problem. The body forces are determined by (myo)fibroblasts that exert forces on their immediate extracellular environment. Since we model the forces by the use of point forces that are possibly not in the H^1 Sobolev space, we scrutinized the mixed finite element method and the homogenization approach. It turns out that these methods do not significantly yield a different behavior for the displacements and area reduction. However, from a computational efficiency point of view, the mixed finite element method turned out to be roughly thirteen times as slow as the direct approach. Furthermore, we analyzed the relation between the immerse boundary approach and the hole approach and it has been shown that the transition from the immerse boundary to the hole approach has a continuous nature with respect to the elasticity in the cellular region. The two methods are equivalent if the stiffness in the cell region is zero. For large numbers of cells, it becomes very beneficial to reduce the polygonal order of the representation

Table 4.6: Time consuming of three area computing methods for different polygons

Polygon	A_{NC}	A_{SL}	A_P
Triangle	$0.81230s$	$0.013478s$	$0.64177s$
Square	$0.82232s$	$0.013588s$	$0.64822s$
Pentagon	$0.80368s$	$0.013579s$	$0.63317s$
Hexagon	$0.81272s$	$0.013680s$	$0.65160s$
Heptagon	$0.81323s$	$0.013810s$	$0.64425s$
Octagon	$0.82601s$	$0.014151s$	$0.65641s$

of the cell boundary. The results indicate that an approximation of a cell boundary by a square is already sufficiently accurate, where the triangular representation is the least time-consuming. Furthermore, the computation of the 'wound' area by the use of connecting all the boundary vertices and the computation of the 'polygon' area is the most efficient procedure.

References

[1] D. Braess. Finite Elements: Theory, Fast Solvers, and Applications in Solid Mechanics. Cambridge University Press, 2007.

[2] B. D. Cumming, D. McElwain, and Z. Upton. A mathematical model of wound healing and subsequent scarring. Journal of The Royal Society Interface, 7(42):19–34, 2009.

[3] S. Enoch and D. J. Leaper. Basic science of wound healing. Surgery (Oxford), 26(2):31–37, 2008.

[4] E. Haertel, S. Werner, and M. Schäfer. Transcriptional regulation of wound inflammation. In Seminars in Immunology, volume 26, pages 321–328. Elsevier, 2014.

[5] D. Koppenol, C. Vuik, and P. van Zuijlen. Biomedical implications from mathematical models for the simulation of dermal wound healing. 2017.

[6] E. Krieger, S. Hornikel, and H. Wehrbein. Age-related changes of fibroblast density in the human periodontal ligament. Head & face medicine, 9(1):22, 2013.

[7] J. Lubliner. Plasticity Theory. Courier Corporation, 2008.

[8] A. L. F. Meister. Generalia de genesi figurarum planarum et inde pendentibus earum affectionibus. 1769.

[9] R. Scott. Finite element convergence for singular data. Numerische Mathematik, 21(4): 317–327, 1973.

[10] F. J. Vermolen and A. Gefen. Semi-stochastic cell-level computational modelling of cellular forces: Application to contractures in burns and cyclic loading. Biomechanics and Modeling in Mechanobiology, 14(6):1181–1195, 2015.

[11] C. Weinberger, W. Cai, and D. Barnett. Lecture notes–elasticity of microscopic structures. ME340–Stanford University, 2005.